An Optimization Framework for the Design of Piezoelectric AFM Cantilevers

Steven Ian Moore*, Michael G. Ruppert, Yuen Kuan Yong

School of Electrical Engineering and Computing, The University of Newcastle, Callaghan, NSW 2308, Australia

Abstract

To facilitate further miniaturization of atomic force microscopy (AFM) cantilevers and to eliminate the standard optical beam deflection sensor, integrated piezoelectric actuation and sensing on the chip level is a promising option. This article presents a topology optimization method for dynamic mode AFM cantilevers that maximizes the sensitivity of an integrated piezoelectric sensor under stiffness and resonance frequency constraints. Included in the formulation is a new material model C-SIMP (connectivity and solid isotropic material with penalization) that extends the SIMP model to explicitly include the penalization of unconnected structures. Example cantilever designs demonstrate the potential of the topology optimization method. The results show, firstly, the C-SIMP material model significantly reduces connectivity issues and, secondly, arbitrary cantilever topologies can produce increases in sensor sensitivity or resonance frequency compared to a rectangular topology.

Keywords: Atomic Force Microscopy, Topology Optimization, Piezoelectric Cantilevers, Connectivity Penalization, Sensitivity Analysis, Microsystems

1. Introduction

1.1. Contributions to AFM Cantilever Design

Atomic force microscopy (AFM) [1] is a pioneering technology in the nanotechnology field which has provided a technological basis for countless methods and applications on the characterization and manipulation of matter on the nanoscale. AFM employs a sharp tip at the end of a microfabricated cantilever to interrogate the surface of a sample. When operated in contact mode, the force exerted by the cantilever on the surface can lead to sample damage, particularly for soft biological samples. Dynamic mode AFM alleviates this issues by oscillating the cantilever at its resonance frequency, impacting the sample only once per cycle which greatly reduces lateral friction forces [2].

High performance dynamic mode AFM cantilevers are characterized by a high resonance frequency and high sensor sensitivity [3]. A high resonance frequency leads to reduced imaging times and reduced sample damage during transients which, for example, facilitates imaging of dynamic biological processes [4]. High sensor sensitivity is a factor in increased image resolution [5]. On the other hand, the stiffness of the cantilever needs to be constrained depending on the sample to be imaged [6]. The development of an optimal mechanical design approach to optimize and trade-off between sensor sensitivity, stiffness, and resonance frequency motivates this work.

Topology optimization [7] has been utilized to design dynamic mode AFM cantilevers with optimal characteristics. When considering sensor sensitivity, designs analyze the response of the optical beam deflection (OBD) method [8] which is the de-facto standard sensor in AFM. The design method presented in the seminal work by Pedersen [9] uses optimization to maximize sensor sensitivity with a constraint on frequency and stiffness, and alternatively, Li et al. [3] uses optimization to maximize a combination of resonance frequency and sensor sensitivity. Other applications of topology optimization in AFM aim to enhance cantilevers for multi-frequency AFM [10] by placing higher-order resonances at integer multiples of the fundamental frequency as to naturally amplify harmonics generated while imaging [11–16].

With all of these optimized designs, only the OBD method is considered for sensing. However the full potential of AFM cantilevers is expected to be achieved by further miniaturization and down-scaling which inevitably renders the OBD sensor infeasible due to limitations in the achievable laser spot size. Additionally, combined AFM/STM high-resolution imaging [17] requires a small footprint and doesn't allow for optical sensing. The only way to resolve this is to use integrated transduction based on piezoresistive or piezoelectric effect [5, 18–20].

This work formulates a topology optimization method to design a piezoelectric AFM cantilever for dynamic mode AFM. The optimization problem maximizes the charge per unit distance of tip deflection of the piezoelectric sensor under resonance frequency and dynamic stiffness constraints. The article outlines the finite element modeling of a laminate piezoelectric structure and the details required to solve the optimization problem robustly. The resulting cantilevers show that the topology optimization method produces designs with improvements in sensor sensitivity or resonance frequency compared to rectangular cantilevers. However, the search for optimal designs

*Corresponding author

Email addresses: steven.i.moore@uon.edu.au (Steven Ian Moore), Michael.Ruppert@newcastle.edu.au (Michael G. Ruppert), yuenkuan.yong@newcastle.edu.au (Yuen Kuan Yong)

is constrained by the dimensions of the design space which fix the length of the cantilever and limit the maximum width of the structure.

1.2. Contributions to Topology Optimization

Numerous optimized piezoelectric structures follow a conventional approach of discretizing the design space using the finite element (FE) method [21–28]. Not only is the FE method used for analysis of the structure, the optimization design variables set the material properties of each element. This leads to a discrete binary problem where a design variable of 1 indicates a solid element, a variable of 0 indicates a void element. However, the referenced works utilize continuous design variables to avoid discrete optimization formulations. This allows for the utilization of gradient based algorithms to solve the optimization problem, such as the method of moving asymptotes [29] or interior point methods [30].

The use of continuous variables, for instance in range 0 to 1, requires the use of an interpolation function for the material properties (elastic modulus, density, piezoelectric coefficient, permittivity) that drives the solution to a binary outcome. The existence of intermediate values for the design variables prevent the fabrication of the structure. The standard interpolation method is the solid isotropic material with penalization (SIMP) method [31] that uses a power law to penalize material properties. The exponents of the power law are heuristically chosen to drive the optimization algorithm to a binary solution. Furthermore in dynamic problems, the selected interpolation must avoid the formation of local modes in low density portions of the FE model [32].

A new interpolation approach is introduced in this work to address the specific requirements of the piezoelectric AFM cantilever design problem. The SIMP method is combined with a formulation that penalizes poorly connected structures. This interpolation method is denoted connectivity and simple isotropic material with penalization (C-SIMP) in this work. The connectivity penalization uses a recently report method of using Poisson's equation to detect connectivity in a topology optimization problem [33, 34]. Penalization using the SIMP method maximizes the piezoelectric sensor sensitivity and avoids local modes while the connectivity penalization drives the solution towards a connected binary structure.

The remainder of this article is outlined as follows. Section 2 formulates the finite element model used to analyze the laminate piezoelectric structure from which the cantilever is formed. Section 3 outlines the C-SIMP material model which penalizes disconnected structures and allows the optimization method to alter the topology. Section 4 introduces a set of structural regulation operations that are applied to the design variables to aid convergence. Section 5 defines the optimization problem, and describes the numerical implementation of the algorithm. Section 6 presents a set of cantilever designs and discusses their performance. Appendix A presents the sensitivity analysis required by the gradient based optimization algorithm.

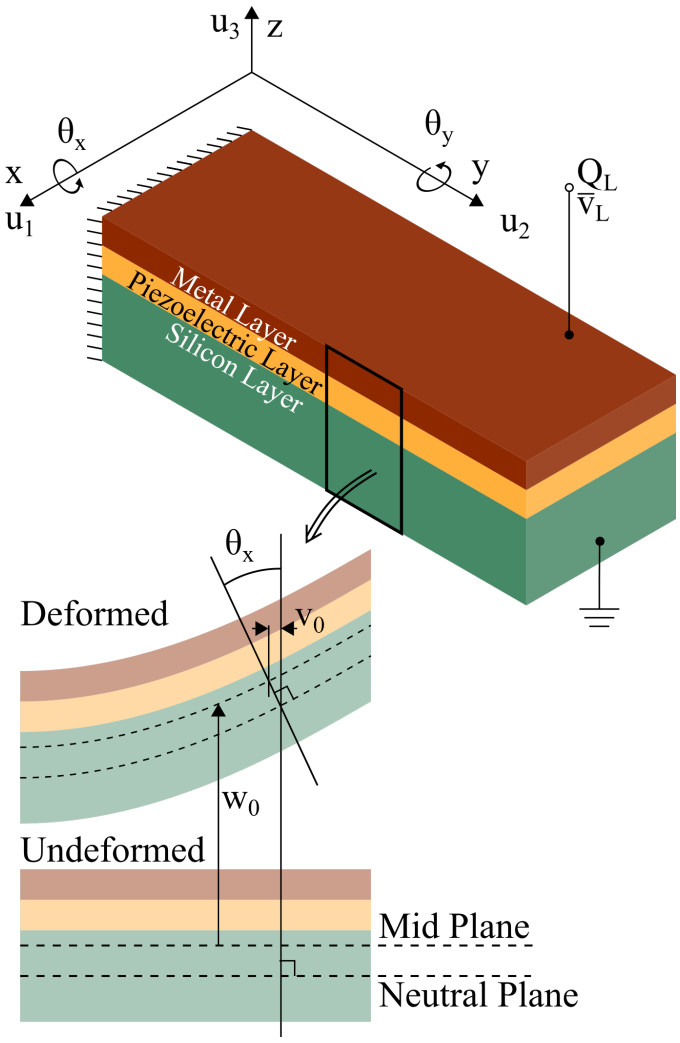

Figure 1: The piezoelectric AFM cantilever is formed from a laminate structure. The laminate plate displacements, rotations, and electrical configuration are shown.

2. Electromechanical Model

The cost function and constraints of the topology optimization method are evaluated using modal analysis of a finite element (FE) model. The model is developed using laminate plate theory to numerically evaluate the resonant behavior of the piezoelectric cantilever. The laminate structure based on the PiezoMUMPS microfabrication process [35], shown in Figure 1, consists of a silicon device layer with a piezoelectric ceramic and metal layer deposited on top for transduction. Section 2.1 introduces the laminate kinematics, electric field distribution, and constitutive equations. These are used to derive energy expressions as a function of the input voltages and output displacements. Hamilton's principle utilizes the energy expressions to derive the dynamic equations of the system. In Section 2.2, the FE method is applied to produce a set of ordinary differential equations for modal analysis.

Table 1: Material properties and dimensions of the layers of the laminate plate [43, 44]. The chosen materials and thickness are from the PiezoMUMPs fabrication process [35].

	Silicon (Si)	Piezoelectric (AlN)	Metal (Al)
Young's Modulus (GPa)	130	300	70
Poisson Ratio	0.28	0.36	0.33
Thickness (um)	10	0.5	1
Density (kg/m^3)	2330	3260	2700
Relative Permittivity	N/A	10.2	N/A
Piezoelectric Coeff. (C/m^2)	N/A	0.58	N/A

2.1. Governing Equations

Numerous investigations into piezoelectric laminate structures employ first-order shear deformation theory (FSDT) to describe the kinematics of the laminate plate [25, 36–39]. The displacement field of the laminate plate is:

$$u_1(x, y, z) = u_0(x, y) + z\theta_y(x, y), \tag{1}$$
$$u_2(x, y, z) = v_0(x, y) - z\theta_x(x, y), \tag{2}$$
$$u_3(x, y, z) = w_0(x, y), \tag{3}$$

where (u_1, u_2, u_3) is the displacement of an infinitesimal piece of material in the structure along the (1) x-axis, (2) y-axis, and (3) z-axis. The laminate displacement parameters are the displacement of the mid-plane (u_0, v_0, w_0) and the rotation of the normal about the x-axis θ_x and y-axis θ_y. The origin of the z-coordinate is the mid-plane of the laminate plate. The standard definitions of infinitesimal strain theory relate the displacement field and strain field [40–42].

A parallel plate capacitive structure is assumed to model the electric field distribution in the piezoelectric layer, which is poled along the z-axis. The silicon and metal layer are considered perfect conductors and the electric field is zero in these layers. The electric field is applied along the z-axis. The potential difference across the piezoelectric layer is $\overline{v}_L$. The electric field distribution is:

$$E_3 = -\frac{\overline{v}_L}{h_L}, \tag{4}$$

where h_L is the thickness of the piezoelectric layer. There is a charge Q_L distributed on the top surface of the piezoelectric layer associated with the voltage $\overline{v}_L$ and the stress in the piezoelectric structure.

The piezoelectric material is modeled by the following constituent equations [40–42]:

$$T = cS - e^T E, \tag{5}$$
$$D = eS + \varepsilon E. \tag{6}$$

c is the elastic modulus matrix, e are the piezoelectric coefficient matrix, and ε is the permittivity matrix. The vectors are the stress T, strain S, electric field E, and electric displacement D. FSDT assumes $S_3 = T_3 = 0$, and poling along the axis three makes $D_1 = D_2 = E_1 = E_2 = 0$ [40–42]. The reduced constitutive equations used for the layers in the laminate plate are:

$$\begin{bmatrix} T_1 \\ T_2 \\ T_4 \\ T_5 \\ T_6 \end{bmatrix} = \begin{bmatrix} c_{11} & c_{12} & 0 & 0 & 0 \\ c_{12} & c_{11} & 0 & 0 & 0 \\ 0 & 0 & c_{44} & 0 & 0 \\ 0 & 0 & 0 & c_{44} & 0 \\ 0 & 0 & 0 & 0 & c_{66} \end{bmatrix} \begin{bmatrix} S_1 \\ S_2 \\ S_4 \\ S_5 \\ S_6 \end{bmatrix} - \begin{bmatrix} e_{31} \\ e_{32} \\ 0 \\ 0 \\ 0 \end{bmatrix} E_3, \tag{7}$$

$$D_3 = \begin{bmatrix} e_{31} & e_{32} & 0 & 0 & 0 \end{bmatrix} \begin{bmatrix} S_1 \\ S_2 \\ S_4 \\ S_5 \\ S_6 \end{bmatrix} + \varepsilon_{33} E_3, \tag{8}$$

where:

$$c_{11} = \frac{Y}{1 - \tilde{\nu}^2}, \tag{9}$$
$$c_{12} = \frac{Y\tilde{\nu}}{1 - \tilde{\nu}^2}, \tag{10}$$
$$c_{44} = \frac{\kappa Y}{2(1 + \tilde{\nu})}, \tag{11}$$
$$c_{66} = \frac{Y}{2(1 + \tilde{\nu})}. \tag{12}$$

Y is Young's modulus, $\tilde{\nu}$ is Poisson's ratio, and $\kappa = \pi^2/12$ is a correction factor. It is assumed the material is homogeneous which implies $e_{31} = e_{32}$. Material properties of the layers of the laminate plate are listed in Table 1. Non-piezoelectric materials are modeled with the piezoelectric coefficient set to zero.

Hamilton's principle is a fundamental physical principle that is able to facilitate the reduction in order of the dynamic equations of a physical system. For an elastic system subjected to conservative forces and charges, Hamilton's principle is mathematically stated as [40–42]:

$$\delta \int_{t_1}^{t_2} \mathcal{T} - \mathcal{H} - \mathcal{V}\, dt = 0, \tag{13}$$

where δ is the variational operator, $\mathcal{T}$ is the kinetic energy of the system, $\mathcal{H}$ is the enthalpy of the system, and $\mathcal{V}$ is the potential energy of the applied forces and charges. In this optimization formulation, only charges applied to the piezoelectric layer are considered. The energies are:

$$\mathcal{T} = \frac{1}{2} \int_\Omega \rho \left(\dot{u}_1^2 + \dot{u}_2^2 + \dot{u}_3^2 \right) d\Omega, \tag{14}$$
$$\mathcal{H} = \frac{1}{2} \int_\Omega T^T S - D^T E\, d\Omega. \tag{15}$$
$$\mathcal{V} = \int_\Omega \rho_q \overline{v}\, d\Omega, \tag{16}$$

where ρ is the material density, and Ω is the domain of the structure, ρ_q is the charge density, and $\overline{v}$ is the voltage.

To develop a model using Hamilton's principle, the kinetic energy, enthalpy, and charge potential energy must be parameterized in terms of the input parameters (the applied voltages/charges) and the unknown outputs (the laminate displacement field). Then, Equation (13) is evaluated for the differential equations of the system.

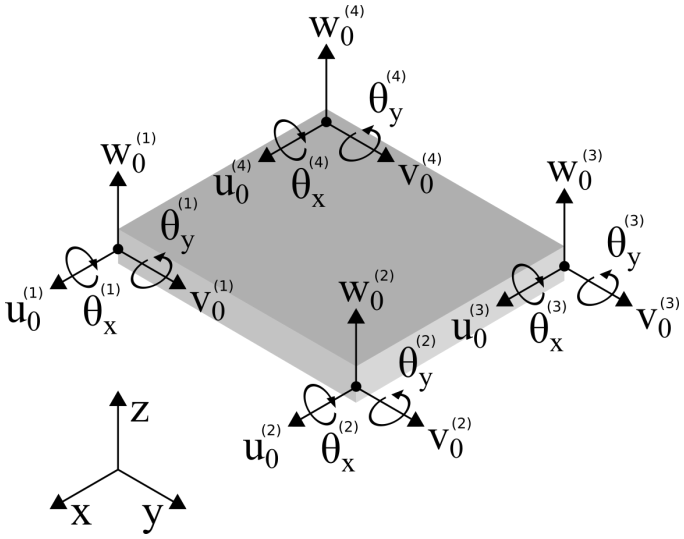

Figure 2: The domain of the structure is discretized into a set of rectangular elements with a node in each corner. Twenty degrees-of-freedom, five at each node, parameterize the mechanical motion of the element. A single electrical DOF parameterizes the voltage across the piezoelectric layer.

2.2. Finite Element Discretization

The finite element model utilizes rectangular four node elements. The laminate displacement field $u_L = [u_0, v_0, w_0, \theta_x, \theta_y]^T$ and the voltage across the piezoelectric layer $\overline{v}_L$ are parameterized by a set of degrees-of-freedom (DOFs). The 20 mechanical DOFs, shown in Figure 2, are:

$$u_e = [u_0^{(1)}, v_0^{(1)}, w_0^{(1)}, \theta_x^{(1)}, \theta_y^{(1)}, \ldots, u_0^{(4)}, v_0^{(4)}, w_0^{(4)}, \theta_x^{(4)}, \theta_y^{(4)}], \quad (17)$$

and $\overline{v}_e$ is the electrical DOF. The mapping from $(u_e, \overline{v}_e)$ to $(u_L, \overline{v}_L)$ is:

$$u_L = N_u u_e, \quad (18)$$

$$\overline{v}_L = \overline{v}_e, \quad (19)$$

where N_u is a matrix of standard bilinear interpolation functions for rectangular four node elements [45]. The mapping from the DOFs $(u_e, \overline{v}_e)$ to the full displacement field $u = [u_1, u_2, u_3]^T$, the strain field $S = [S_1, S_2, S_4, S_5, S_6]^T$, and the electric field E are:

$$u = B_u u_e, \quad (20)$$

$$S = B_S u_e, \quad (21)$$

$$E = -B_E \overline{v}_e, \quad (22)$$

where the mechanical DOFs to displacement matrix B_u is derived from combining Equations (18) and (19) and Equations (1) to (3), the mechanical DOFs to strain matrix B_s is formed from partial derivatives of B_u [40–42], and the electrical DOF to electric field matrix B_E is derived from a combination of Equations (4), (18) and (19). The expressions in Equations (20) to (22) are substituted into the formulas for the kinetic energy (Equation (14)) and enthalpy (Equation (15)) for the evaluation of Hamilton's principle. To evaluate the potential energy of the externally applied charge, a charge Q_e is applied to the piezoelectric layer at voltage $\overline{v}_e$. The evaluation of Hamilton's principle in Equation (13) and the assembly of the complete finite element model yields:

$$\begin{bmatrix} M_{uu} \\ 0 \end{bmatrix} \ddot{u} + \begin{bmatrix} K_{uu} & K_{uv} \\ -K_{uv}^T & K_{vv} \end{bmatrix} \begin{bmatrix} u \\ v_L \end{bmatrix} = \begin{bmatrix} 0 \\ Q_L \end{bmatrix}, \quad (23)$$

where u is the complete set of mechanical DOFs, $v_L = v_e$ as there is only one electrical DOF in the entire system, and Q_L is the sum of charges from all elements. The mass matrix M_{uu}, stiffness matrix K_{uu}, piezoelectric matrix K_{uv}, and capacitance matrix K_{vv} are formed with assembly of the element matrices [23]:

$$K_{uu}^e = \int_{\Omega_e} B_S^T c B_S \, d\Omega, \quad (24)$$

$$K_{uv}^e = \int_{\Omega_e} B_S^T e B_E \, d\Omega, \quad (25)$$

$$K_{vv}^e = \int_{\Omega_e} B_E^T \varepsilon B_E \, d\Omega, \quad (26)$$

$$M_{uu}^e = \int_{\Omega_e} \rho B_u^T B_u \, d\Omega. \quad (27)$$

Assuming a harmonic solution for the displacement $u = \phi \cos(\omega t)$ and no applied voltage, which is the case when instrumenting the cantilever with a charge amplifier, the differential equation is solved with an eigenvalue problem:

$$(\lambda M_{uu} - K_{uu})\, \phi = 0, \quad (28)$$

where $\lambda = \omega^2$ is the eigenvalue and ϕ is the eigenvector, referred to as the mode shape in this work. Solutions exist for a countably infinite set of eigenvalues. This work focuses on the first mode, that is the solution with the lowest eigenvalue λ_1 and its associated mode shape ϕ_1. The optimization problem utilizes the solution to the eigenvalue problem and the FE element model matrices in Equation (23) to compute the cost function and constraints.

3. C-SIMP Material Model

To alter the FE model and the topology, a parameter for each element, denoted the pseudo-density $\bar{\rho}_i \in [0, 1]$, parameterizes the structure. A value of 0 indicates a void element and a value of 1 indicates a solid element. To facilitate continuous optimization variables, the pseudo-densities vary in the range 0 to 1. A continuous material model defines the material properties of the element for an intermediate value of the pseudo-density. This work defines an extension to the SIMP material model denoted connectivity and SIMP (C-SIMP). The material model is:

$$c_i = \exp(-q_e \mu_i) \bar{\rho}_i^{\,p_e} c_0, \quad (29)$$

$$e_i = \exp(-q_p \mu_i) \bar{\rho}_i^{\,p_p} e_0, \quad (30)$$

$$\varepsilon_i = \exp(-q_c \mu_i) \bar{\rho}_i^{\,p_c} \varepsilon_0, \quad (31)$$

$$\rho_i = \exp(-q_d \mu_e) \bar{\rho}_i^{\,p_d} \rho_0. \quad (32)$$

The material properties of the i^{th} element are: the elastic modulus matrix c_i, the piezoelectric coefficient matrix e_i, is the permittivity matrix ε_i, and the density ρ_i. $(c_0, e_0, \varepsilon_0, \rho_0)$ are the

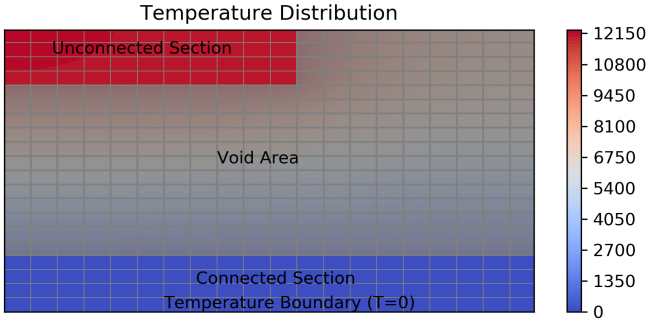

Figure 3: In the example shown, connectivity analysis is applied to a structure with an unconnected section in the the top-left corner. The temperature distribution provides a measure of the connectivity – closer to 0 is more connected to the boundary.

nominal material properties of a solid element. μ_i is the connectivity penalty of the element which quantifies how connected the element is to the base of the cantilever. (p_e, p_p, p_c, p_d) are the SIMP penalization factors and (q_e, q_p, q_c, q_d) are the connectivity penalization factors. The penalization factors are used to tune the implementation to drive the solution to a binary structure.

The connectivity penalties are evaluated using the virtual temperature method, previously used to prevent the formation of voids in a structure during topology optimization [33, 34]. A modification to this method is formulated to penalize unconnected structures. A secondary thermal system is created and the parameters of the thermal system are tuned by the pseudo-densities. Solid elements exhibit excellent thermal conductivity and have a heat source, while void elements exhibit low conductivity and have no heat source. A thermal boundary exists at the fixed end of the cantilever. Unconnected sections of the structure attain a high steady-state temperature in the secondary thermal system. The temperature field across the structure is used to evaluate the connectivity penalties for each element. Poisson's equation describes the behavior of the thermal system:

$$\nabla(\overline{k}\nabla\overline{T}) + \overline{q} = 0, \tag{33}$$

where $\overline{k}$ is the thermal conductivity, $\overline{T}$ is the temperature, and $\overline{q}$ is the heat source. The finite element method is used to evaluate the equation. The thermal system uses the same mesh and interpolation functions that are used for the electromechanical system. The temperature field across an element is:

$$\overline{T}(x, y) = N_\tau(x, y)\tau_i, \tag{34}$$

where N_τ is a matrix of interpolation functions, and τ_i are the four temperature DOFs, one at each node of the rectangular element. The thermal conductivity and heat source for each element are a function of the pseudo-density:

$$\overline{k}_i = \overline{k}_{max}\bar{\rho}_i + (1 - \bar{\rho}_i)\overline{k}_{min}, \tag{35}$$

$$\overline{q}_i = \overline{q}_{max}\bar{\rho}_i. \tag{36}$$

The method of weighted-residuals is used to derive the weak form of Poisson's equation. The element matrices are:

$$K^e_\tau = \overline{k}_i \int_{\Omega_e} \nabla N^T_\tau \nabla N_\tau \, d\Omega_e, \tag{37}$$

$$\overline{q}^e_\tau = \overline{q}_i \int_{\Omega_e} N^T_\tau \, d\Omega_e. \tag{38}$$

These matrices are used to form the fully assembled system:

$$K_\tau \tau = \overline{q}_\tau, \tag{39}$$

where K_τ is the conduction matrix, $\overline{q}_\tau$ is the source matrix, and τ are the temperature DOFs. With four DOFs per element, the connectivity penalty is taken as the average, that is:

$$\mu_i = \text{mean}(\tau_i), \tag{40}$$

which is the temperature at the center of the element. Figure 3 shows an example of the connectivity analysis on a binary structure with an unconnected section. For the evaluation of Equations (35) and (36), $\overline{k}_{max} = \overline{q}_{max} = 1$ and $\overline{k}_{min} = 0.01$. The temperature distribution from the evaluation of Poisson's equation shows a significant magnitude in the temperature metric of the unconnected section indicating a highly disconnect area in the topology.

4. Structural Regularization

The pseudo-densities required by the C-SIMP model are computed by applying structural regularization to the optimization design variables. Regularization refers to operations that drive the design to a realizable structure and minimizes mesh-dependent issues [46]. In this optimization method, three regularization operators are employed. An operator to enforce symmetry, a low-pass filter to eliminate checkerboard patterns, and a projection operator to penalize intermediate pseudo-densities. The combined set of operators take x_d and return $\bar{\rho}$ that are used to assemble the FE model. The effect of the regularization operators is visualized in Figure 4.

Symmetry Operator. To enforce symmetry, elements mirrored along the axis of the cantilever share the same pseudo-density. Each pair of mirrored elements is associated with a single design variable in x_d. If the element lies on the axis of the cantilever, it is not paired with any other element. The symmetry operator G_s is a sparse binary non-invertible linear operator which maps the x_d to $\bar{\rho}_a$. While non-invertible, an approximate inverse operator is defined by taking the average pseudo-density of each pair of mirrored elements to return the design variable:

$$x_d = \alpha_s G^T_s \bar{\rho}_a, \tag{41}$$

where α_s is a diagonal matrix whose diagonal terms are 0.5 if the design variable is associated with a pair of elements, and 1 if the design variable is associated with a single element on the axis of the cantilever. The inverse operator is used to create the initial design parameters for the optimization method.

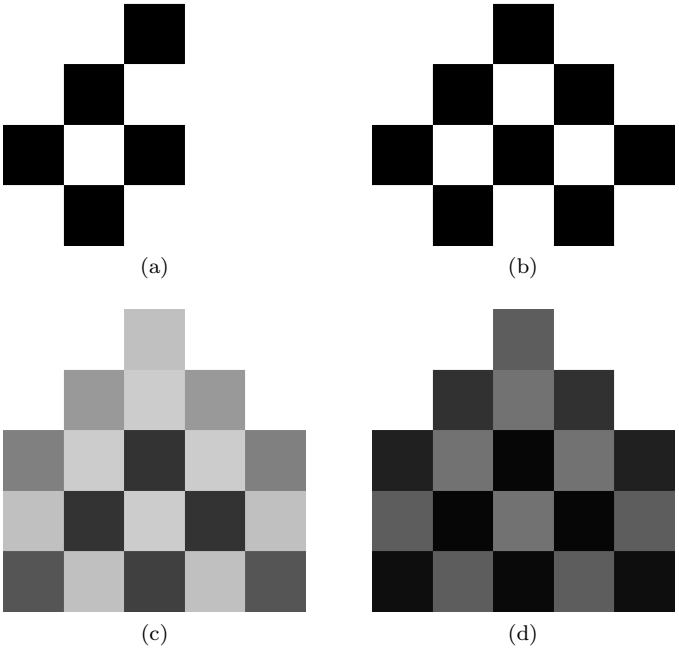

Figure 4: The effects of structural regularization. In this example, the regularization is applied to a checkerboard-like structure (a) in a 5x5 element design space. Black is a solid element, white is a void element, and gray is an intermediate element. (b) The symmetry operator mirrors the structure in the second half of the design space. (c) The density filter eliminates the infeasible checkerboard pattern, however, it creates intermediate pseudo-densities. (d) The projection operator moves intermediate pseudo-densities back towards solid.

Density Filter. Next the pseudo-densities from the symmetry operator are filtered. Filtering of the densities encourages structural connectivity and prevents the formation of checkerboard patterns in the structure. The density filter employed in this work is given by [23, 46–48]:

$$\bar{\rho}_{b,j} = \frac{1}{\sum_{i \in N_j} H_{ji}} \sum_{i \in N_j} H_{ji} \bar{\rho}_{a,i}, \tag{42}$$

where H_{ji} are the filter coefficients and N_j is the set of elements neighboring element j. The coefficients H_{ji} are defined as:

$$H_{ji} = r_{min} - \Delta(j, i), \tag{43}$$

where r_{min} is a parameter denoted the filter radius, and $\Delta(j, i)$ is the distance between element i and element j. The set of neighboring elements to the element j is defined as:

$$N_j = \{i : r_{min} - \Delta(j, i) > 0\} \tag{44}$$

The filter is a linear operator and its matrix form G_d is sparse for small r_{min}. An undesirable side-effect of the the density filter is that it tends to produce intermediate pseudo-densities along the edge of the structure.

Projection. The issue of intermediate pseudo-densities produced by the density filter is alleviated with the projection operator. It is a diagonal non-linear operator that skews intermediate pseudo-densities towards solid. While a step function would be ideal, the operator needs to be differentiable for the optimization algorithm to be well-defined. A smoothed version of the step function is used:

$$\bar{\rho} = 1 - \exp(-\beta \bar{\rho}_b) + \bar{\rho}_b \exp(-\beta), \tag{45}$$

where β tunes the steepness of the function.

5. Optimization Strategy

5.1. Problem Definition

The electromechanical-model, C-SIMP material model, and structural regularization introduced in previous sections are utilized for an optimal electro-mechanical design of a piezoelectric AFM cantilever. The aim is to produce a cantilever with maximum sensor sensitivity, that is charge produced for unit of tip displacement (Cm^{-1}), at the first resonance frequency. Constraints on the stiffness and frequency are required to make the optimization problem well defined. Stiffer cantilevers stress the piezoelectric ceramic more producing more charge for the same displacement, therefore an upper bound on the stiffness is required to prevent extremely stiff cantilevers from forming. Large low frequency cantilevers with greater amounts of piezoelectric ceramic can produce more charge, therefore a lower bound on frequency is required to prevent extremely low frequency cantilevers from forming. As such the optimization problem is defined as:

$$\begin{aligned} \min \quad & -\eta_1, && (46)\\ \text{s.t.} \quad & k_1 < k_0, && (47)\\ & f_1 > f_0, && (48) \end{aligned}$$

where η_1 is the sensor sensitivity of the first mode, k_1 is the dynamic stiffness of the first mode, f_1 is the resonance frequency of the first mode, k_0 is an upper bound on the stiffness, and f_0 is a lower bound on the resonance frequency. The objective function is:

$$-\eta_1 = \frac{K_{uv}^T \phi_1}{G_{uu} \phi_1}, \tag{49}$$

where G_{uu} is a linear operator that returns the displacement at the tip of the cantilever. The numerator of Equation (49) is the charge produced by the piezoelectric ceramic and the denominator is the deflection of the tip. The dynamic stiffness of the cantilever is:

$$k_1 = \frac{\phi_1^T K_{uu} \phi_1}{(G_{uu} \phi_1)^2}, \tag{50}$$

and the resonance frequency of the first mode is:

$$f_1 = \frac{\sqrt{\lambda_1}}{2\pi}. \tag{51}$$

5.2. Implementation

The diagram of the software architecture of the topology optimization method is shown in Figure 5. The interior point method using the IPOPT library [30] is employed to solve the

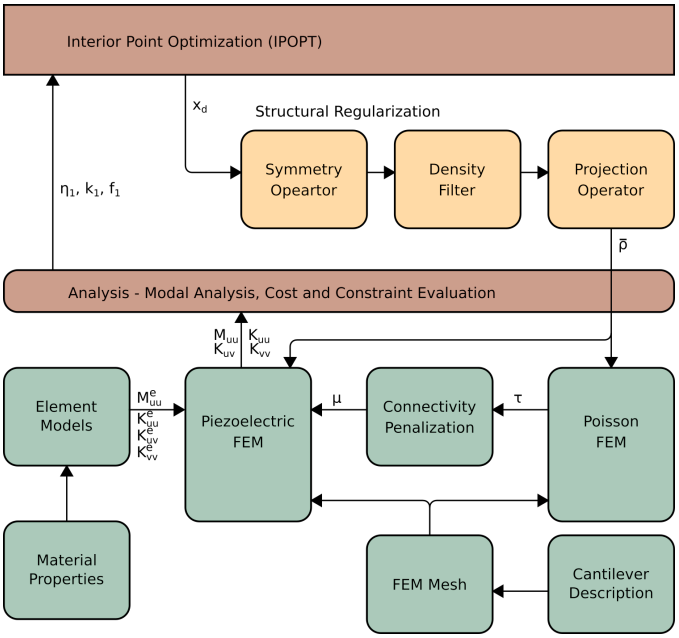

Figure 5: The software architecture of the topology optimization method to design the piezoelectric AFM cantilever.

Table 2: The C-SIMP penalization factors employed to drive the solution to a binary structure.

p_e	p_p	p_d	p_d	q_e	q_p	q_c	q_d
1	5	0	3	0	0.3	0	0

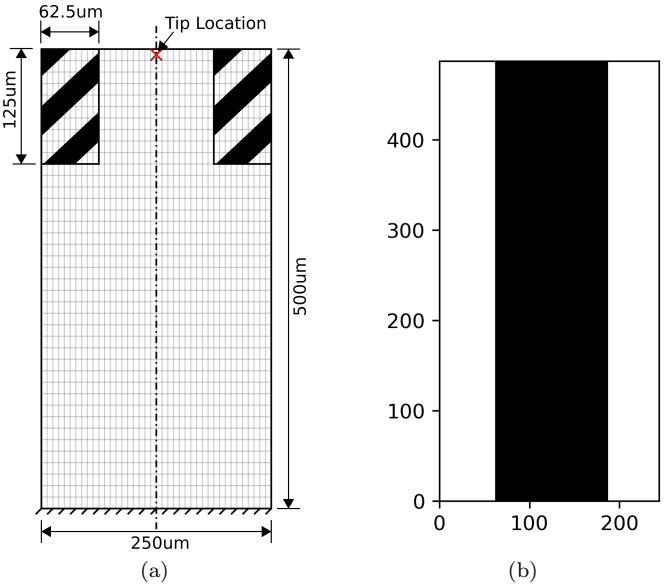

Figure 6: (a) The design space in which the piezoelectric AFM cantilever is formed. The dimensions, the FE mesh, tip location, and exclusion zones are indicated. (b) The initial cantilever design used to initialize the IPOPT optimization algorithm. Units are in µm.

topology optimization problem. The execution of the IPOPT algorithm produces x_d which is transformed to $\bar{\rho}$ with structural regularization, outlined in Section 4. With the pseudo-densities, the connectivity penalization is evaluated and then the piezoelectric FE model is assembled. Finally the objective and constraints are evaluated using the FE model. The size and shape of the initial finite element model defines the size of the design space in which the cantilever can form. Furthermore, sensitivity analysis, that is the computation of the gradients of the objective and constraints, is required for the interior point method. Sensitivity analysis is outlined in Appendix Appendix A. The steps of the algorithm are:

1. Initialize the operators used in the finite element analysis, sensitivity analysis, structural regularization, and connectivity penalization.
2. From the pseudo-densities of an initial binary structure use Equation (41) to compute an initial x_d.

Repeat:

3. Execute a step of the IPOPT optimization algorithm to update the x_d.
4. Calculate $\bar{\rho}$ using structural regularization.
5. Assemble the secondary thermal system to evaluate the connectivity penalties μ.
6. Assemble piezoelectric FE model using the C-SIMP material model for the mass, stiffness, piezoelectric, and capacitance matrices ($M_{uu}, K_{uu}, K_{uv}, K_{vv}$).
7. Perform modal analysis and compute the objective and constraints.
8. Calculate the sensitivity of the objective function and constraints with respect to x_d.

Terminate:

9. When the percentage change in the objective is small return solution.

The penalization factors employed in this method are listed in Table 2. Heavy penalization on the piezoelectric coefficient via (p_p, q_p) is used due to the direct dependence of the objective function on the piezoelectric matrix K_{uv}. With the constraint on frequency indirectly constraining the amount of mass present, the optimization algorithm finds greater efficiency in using fully solid elements to maximize the sensor sensitivity. The density is penalized heavier than the elasticity to keep void parts of the structure stiff and light during optimization. This prevents the formation of low frequency local modes which masks the true first mode of the cantilever in modal analysis [32].

6. Results and Discussion

6.1. Comparison with Rectangular Solutions

To examine the performance of the topology optimization method, a set of cantilevers are designed with various stiffness constraints k_0 and frequency constraints f_0. To summarize, the objective of the topology optimization method is to maximize the sensor sensitivity η_1 with a upper bound on the cantilever

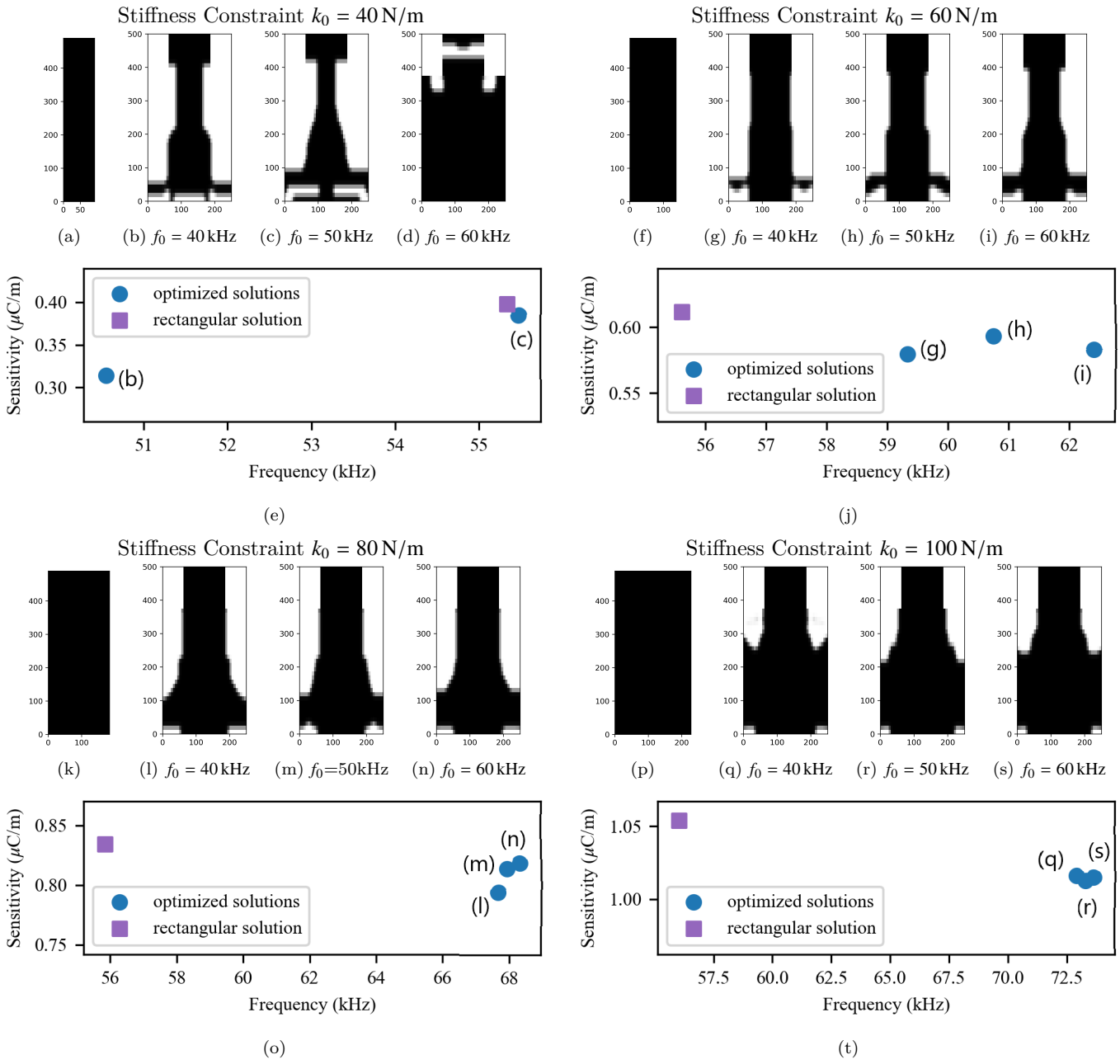

Figure 7: The cantilevers are grouped by stiffness constraint k_0. (b-d,g-i,l-n,q-s) Are the topology of the optimized cantilever designs. (a,f,k,p) Are optimized rectangular cantilevers under a stiffness constraint. (e,j,o,t) Show the frequency and sensitivity of each design.

stiffness $k_1 < k_0$ and a lower bound on the resonance frequency $f_1 > f_0$.

The optimized cantilevers are formed in a design space 250 µm wide and 500 µm long, discretized into 6.25 µm by 12.5 µm elements as shown in Figure 6(a). Rectangular sections of 62.5 µm wide by 125 µm are removed from the upper right and left corner of the design space. This is a heuristic that was found to minimize the likelihood of a torsional mode becoming the lowest frequency mode and disrupting the execution of the topology optimization method. The mode shapes are normalized to the displacement at the tip which lies on the cantilever axis and half an element length from the edge of the design space. The first mode of a cantilever filling this entire design space has a stiffness of 109.9 N m^{-1}, a frequency of 69.27 kHz, and a sensitivity of 1.12 µC/m.

A rectangular cantilever, shown in Figure 6(b), is used as the initial condition of the optimization problem. This cantilever has a mode 1 resonance frequency of 55.5 kHz, mode 1 dynamic stiffness of 54.13 N/m, and a sensor sensitivity of 0.547 µC/m.

Figure 7 shows the set of cantilevers that was produced by the topology optimization method, along with a set of rectangular reference cantilevers.

In all figures presenting the cantilevers, black indicates a

solid element, white a void element, and gray an intermediate element. Cantilever dimensions are in µm, and the fixed boundary is along the bottom edge of the figure. The constraints on each cantilever are permutations of a frequency constraint of f_0 = (40 kHz, 50 kHz, 60 kHz) and a stiffness constraint of k_0 = (40 N/m, 60 N/m, 80 N/m, 100 N/m). The rectangular cantilevers have a fixed 500 µm length, and the width is the design parameter. The rectangular designs are optimized without a frequency constraint.

The first conclusion is that there is a strong correlation between the dynamic stiffness of the cantilevers and the sensor sensitivity. The stiffer cantilevers stress the piezoelectric ceramic more for the same displacement producing more charge. For all cantilever solutions, the stiffness of the cantilever increases until it hits the stiffness constraint of the optimization problem. As cantilevers with the same stiffness constraint k_0 attain the same dynamic stiffness, cantilevers are grouped for comparison by stiffness in Figure 7.

As the dynamic stiffness approaches the constraint, the topology optimization method continues to add mass in areas where the stress is small. This additional mass contributes insignificantly to the dynamic stiffness but adds a small amount of charge thereby reducing the objective function. The addition of extra mass reduces the resonance frequency, thus justifying the frequency constraint. In addition, this process results in wing-like structures appearing off the side of the main cantilever structure. These wings tend to lower the frequency of torsional modes, especially if the they are at the tip of the structure. The elimination of these wing-like structures motivates restricting the design space near the tip of the cantilever as shown in Figure 6(a).

When the designs are benchmarked against the reference rectangular cantilevers having the same stiffness constraint and same length, the charge sensitivities of the optimized designs are less than that of rectangular reference cantilevers. Hence from a charge sensitivity maximization perspective, the optimization method does not lead to improvements. This also suggests that the problem is non-convex as optimization problem does not converge towards the more optimal rectangular designs. However, with respect to the resonance frequency of the designs, the optimized cantilevers have higher frequencies which is desirable for high speed AFM imaging. The rectangular cantilevers all have a frequency of approximately 55 kHz while the optimized cantilevers with stiffness constraint greater than 60 N/m all had higher frequencies with the highest frequency attained being 73 kHz.

6.2. *The Effect of the Connectivity Penalization*

Connectivity penalization significantly reduces the chance of an infeasible solution due to the presence of unconnected sections of the structure. Examining the set of cantilevers designed with no connectivity penalization in Figure 8, six cantilevers exhibited unconnected structural sections. In contrast, there is only one unconnected structure in the set with connectivity penalization in Figure 7. Connectivity issues are more likely to occur for solutions for higher frequency constraints f_0 or lower stiffness constraints k_0.

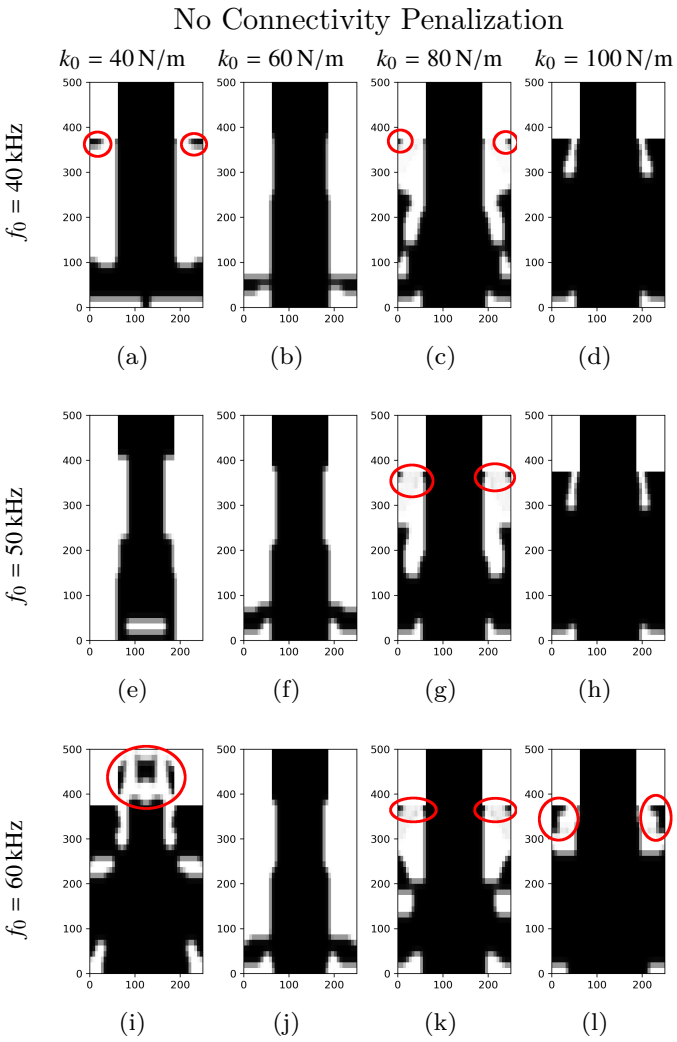

Figure 8: (a-l) These cantilevers are designed without connectivity penalization. Unconnected structural elements are circled in red.

Examining the one unconnected solution (Figure 7(d)) with connectivity penalization, it is the cantilever designed under the strictest frequency and stiffness constraints (f_0 = 60 kHz, k_0 = 40 N/m). When the constraints are too strict, the optimization algorithm justifies some connectivity violation. The amount of connectivity violation an optimal solution allows is tuned by the connectivity penalization factors (q_e, q_p, q_c, q_d).

The unconnected sections in the results in Figure 8 tend to be small and could be manually removed. This manual process, which may not be applicable to other topology optimization problems, is avoided when using the C-SIMP material model.

6.3. *The Effect of the Design Space Dimensions*

It was found that the chosen design space limited the possible range of stiffness constraints that could be applied in the topology optimization method. The upper limit of the stiffness tends to be a function of the dimensions of the design space. Raising the stiffness constraint leads to more of the design space being filed with more solid elements. There would be a constraint value in which the entire design space becomes solid.

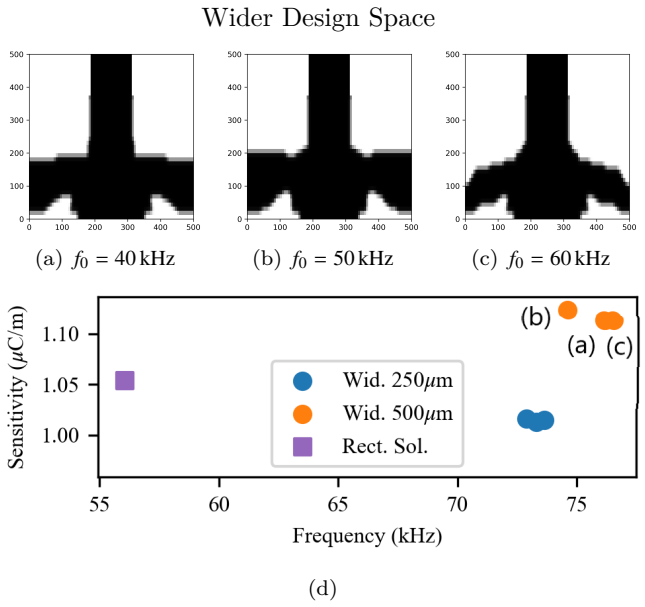

Figure 9: (a-c) Optimized cantilevers with a wider design space for a stiffness constraint of k_0 = 100 N/m. (d) Shows the frequency and sensitivities of these designs, and those in Figure 7(p-s).

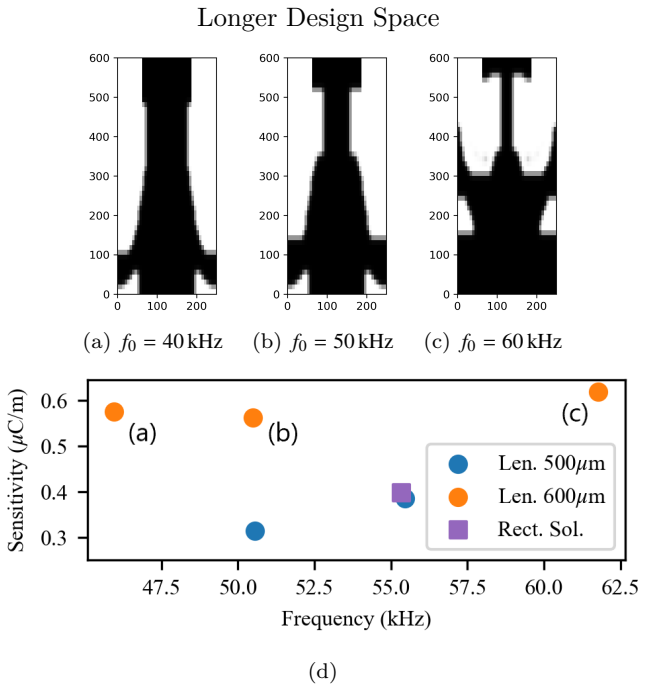

Figure 10: (a-c) Optimized cantilevers with a longer design space with stiffness constraint k_0 = 40 N/m. (d) Compares the frequency and stiffness of these designs to those in Figure 7(a-c).

Lower values in dynamic stiffness lead to connectivity issues. The range of possible dynamic stiffnesses that can be attained is set by altering the design space.

To examine the effect of altering the design space, the cantilevers in Figure 9 are solutions with stiffness k_0 = 100 N/m for a design space width of 500 µm. Compared to the cantilevers formed in the 250 µm wide design space in Figure 7, an improvement in performance for the cantilevers with the 500 µm wide design space. With the wider design space, more of the mass of the cantilever was distributed towards the base of the cantilever leading to a marginally higher resonance frequency and an increase in sensor sensitivity is attained. In addition, there is a significant improvement over the rectangular references cantilevers in Figure 7(p). This suggests a search over the design space dimensions is also required to find more optimal solutions. Setting the width such that the optimized topology isn't constrained would eliminate this effect. However, increasing the width of the design space increases the computation time due to the additional elements added to the design space.

The effect of the length of the design space was explored for optimization problems with a low stiffness constraint. Longer cantilevers are generally softer therefore lower stiffness constraints should be easier to satisfy. The design problems for the cantilevers with k_0 = 40 N/m were re-executed with the length of the design space increased from 500 µm to 600 µm. The results are shown in Figure 10. The longer design space eliminates the connectivity issues at the expense of lower frequency cantilevers. In addition, the longer cantilevers have higher charge sensitivities than the shorter cantilevers with the same stiffness constraints. The increase in the design space length leads to a reduction in frequency and an increase in sensor sensitivity while the stiffness k_1 attains equality to the stiffness constraint k_0. This suggests that the optimal cantilever is one where $f_0 = f_1$ and $k_0 = k_1$. To attain this solution the topology optimization method present in this work needs to be modified to eliminate the dependence of the fixed design space from the solution.

7. Conclusions

Topology optimization has addressed a broad range of design problems. This article builds upon this body of work to address the specific requirements for the design problem of a piezoelectric cantilever for dynamic mode AFM. In particular, the introduced material model C-SIMP allows for SIMP penalization to target the minimization of the objective function while the connectivity penalization minimizes connectivity and intermediate pseudo-density issues. The benefits of this material model was demonstrated with significantly less unconnected structures between the two sets of cantilever designs, one without and one with connectivity penalization.

The presented topology optimization method produced a number of optimized piezoelectric cantilevers for dynamic mode AFM. With previous reported topology optimization methods for AFM cantilevers focusing on optical sensing, the piezoelectric sensing focus of this method provides a new avenue for the application of topology optimization to AFM. The

results presented in this work suggest that modest improvements in either sensor sensitivity or resonance frequency can be achieved with more arbitrary cantilever topologies compared to rectangular topologies. A major constraint in the current method is the constraining effect of the design space dimensions. In particular the tip location, the point at which mode shapes are normalized, is fixed within the design space. An extension that facilitates a variable tip location or cantilever length would provide greater flexibility to search for an optimal solution.

With only modest improvements attained and the limitations of the design space, the value of this design method appears less in the presented results and more in the potential to provide a basis to develop alternative topology optimization solutions for dynamic piezoelectric devices. With the presented piezoelectric modeling, dynamic analysis, C-SIMP material model and other implementation details, this method shall be extended for the design of cantilevers for multi-frequency AFM where the complex interaction between the topology and multiple structural are beyond intuitive electro-mechanical design.

References

[1] G. Binnig, C. F. Quate, C. Gerber, Atomic force microscope, Phys. Rev. Lett. 56 (9) (1986) 930–933.

[2] R. Garcia, R. Perez, Dynamic atomic force microscopy methods, Surface Science Reports 47 (6–8) (2002) 197 – 301.

[3] Z. Li, T. Shi, Q. Xia, Design optimization of high performance tapping mode afm probe, Microsystem Technologies (2017) 1–9.

[4] M. Shibata, T. Uchihashi, T. Ando, R. Yasuda, Long-tip high-speed atomic force microscopy for nanometer-scale imaging in live cells, Scientific Reports 5.

[5] J. C. Doll, B. L. Pruitt, Design of piezoresistive versus piezoelectric contact mode scanning probes, Journal of Micromechanics and Microengineering 20 (9) (2010) 095023.

[6] J. E. Sader, I. Larson, P. Mulvaney, L. R. White, Method for the calibration of atomic force microscope cantilevers, Review of Scientific Instruments 66 (7) (1995) 3789–3798.

[7] J. D. Deaton, R. V. Grandhi, A survey of structural and multidisciplinary continuum topology optimization: post 2000, Structural and Multidisciplinary Optimization 49 (1) (2014) 1–38.

[8] G. Meyer, N. M. Amer, Novel optical approach to atomic force microscopy, Applied Physics Letters 53 (12) (1988) 1045–1047.

[9] N. L. Pedersen, Design of cantilever probes for atomic force microscopy (AFM), Engineering Optimization 32 (3) (2000) 373–392.

[10] R. Garcia, E. T. Herruzo, The emergence of multifrequency force microscopy, Nat Nano 7 (4) (2012) 217–226.

[11] Q. Xia, T. Zhou, M. Wang, T. Shi, Shape and topology optimization for tailoring the ratio between two flexural eigenfrequencies of atomic force microscopy cantilever probe, Frontiers of Mechanical Engineering 9 (1) (2014) 50–57.

[12] J. Cai, Q. Xia, Y. Luo, L. Zhang, M. Y. Wang, A variable-width harmonic probe for multifrequency atomic force microscopy, Applied Physics Letters 106 (7).

[13] B. Zhu, S. Zimmermann, X. Zhang, S. Fatikow, A systematic method for developing harmonic cantilevers for atomic force microscopy, J. Mech. Des 139 (1) (2016) 012303.

[14] J. Cai, M. Y. Wang, Q. Xia, Y. Luo, Optimal design of a tapping-mode atomic force microscopy cantilever probe with resonance harmonics assignment, Engineering Optimization 49 (1) (2017) 43–59.

[15] S. I. Moore, Y. K. Yong, Design and characterisation of cantilevers for multi-frequency atomic force microscopy, IET Micro Nano Letters 12 (5) (2017) 315–320.

[16] S. I. Moore, M. G. Ruppert, Y. K. Yong, Arbitrary placement of afm cantilever higher eigenmodes using structural optimization, in: 2018 International Conference on Manipulation, Automation and Robotics at Small Scales (MARSS), 2018, pp. 1–6.

[17] D. Ebeling, Q. Zhong, S. Ahles, L. Chi, H. A. Wegner, A. Schirmeisen, Chemical bond imaging using higher eigenmodes of tuning fork sensors in atomic force microscopy, Applied Physics Letters 110 (18) (2017) 183102.

[18] M. Li, H. X. Tang, M. L. Roukes, Ultra-sensitive nems-based cantilevers for sensing, scanned probe and very high-frequency applications, Nat Nano 2 (2007) 114–120.

[19] S. I. Moore, M. G. Ruppert, Y. K. Yong, Multimodal cantilevers with novel piezoelectric layer topology for sensitivity enhancement, Beilstein Journal of Nanotechnology 8 (2017) 358–371.

[20] M. G. Ruppert, S. I. Moore, M. Zawierta, A. Fleming, G. Putrino, Y. K. Yong, Multimodal atomic force microscopy with optimized higher eigenmode sensitivity using on-chip piezoelectric actuation and sensing, Nanotechnology.

[21] E. C. N. Silva, N. Kikuchi, Design of piezoelectric transducers using topology optimization, Smart Materials and Structures 8 (3) (1999) 350.

[22] Y. Ha, S. Cho, Design sensitivity analysis and topology optimization of eigenvalue problems for piezoelectric resonators, Smart Materials and Structures 15 (6) (2006) 1513.

[23] P. Nakasone, E. Silva, Dynamic design of piezoelectric laminated sensors and actuators using topology optimization, Journal of Intelligent Material Systems and Structures 21 (16) (2010) 1627–1652.

[24] W. M. Rubio, G. H. Paulino, E. C. N. Silva, Tailoring vibration mode shapes using topology optimization and functionally graded material concepts, Smart Materials and Structures 20 (2) (2011) 025009.

[25] L. A. M. Mello, C. Y. Kiyono, P. H. Nakasone, E. C. N. Silva, Design of quasi-static piezoelectric plate based transducers by using topology optimization, Smart Materials and Structures 23 (2) (2014) 025035.

[26] A. Takezawa, M. Kitamura, S. Vatanabe, E. C. N. Silva, Design methodology of piezoelectric energy-harvesting skin using topology optimization, Structural and Multidisciplinary Optimization 49 (2) (2014) 281–297.

[27] L. P. da Silva, W. Larbi, J.-F. Deü, Topology optimization of shunted piezoelectric elements for structural vibration reduction, Journal of Intelligent Material Systems and Structures 26 (10) (2015) 1219–1235.

[28] B. Zhu, X. Zhang, Y. Zhang, S. Fatikow, Design of diaphragm structure for piezoresistive pressure sensor using topology optimization, Structural and Multidisciplinary Optimization 55 (1) (2017) 317–329.

[29] K. Svanberg, The method of moving asymptotes—a new method for structural optimization, International Journal for Numerical Methods in Engineering 24 (2) (1987) 359–373.

[30] A. Wächter, L. T. Biegler, On the implementation of an interior-point filter line-search algorithm for large-scale nonlinear programming, Mathematical Programming 106 (1) (2006) 25–57.

[31] M. P. Bendsoe, O. Sigmund, Topology Optimization: Theory, Methods and Applications, Springer, 2003.

[32] N. Pedersen, Maximization of eigenvalues using topology optimization, Structural and Multidisciplinary Optimization 20 (1) (2000) 2–11.

[33] S. Liu, Q. Li, W. Chen, L. Tong, G. Cheng, An identification method for enclosed voids restriction in manufacturability design for additive manufacturing structures, Frontiers of Mechanical Engineering 10 (2) (2015) 126–137.

[34] Q. Li, W. Chen, S. Liu, L. Tong, Structural topology optimization considering connectivity constraint, Structural and Multidisciplinary Optimization 54 (4) (2016) 971–984.

[35] A. Cowen, G. Hames, K. Glukh, B. Hardy, PiezoMUMPs Design Handbook, MEMSCAP Inc., 1st Edition (2014).

[36] J. N. Reddy, Energy Principles and Variational Methods in Applied Mechanics, John Wiley & Sons, 2002.

[37] Z. Kang, L. Tong, Integrated optimization of material layout and control voltage for piezoelectric laminated plates, Journal of Intelligent Material Systems and Structures 19 (8) (2008) 889–904.

[38] A. J. M. Ferreira, Matlab Codes for Finite Element Analysis: Solids and Structures, Springer, 2009.

[39] X. Zhang, Z. Kang, Topology optimization of piezoelectric layers in plates with active vibration control, Journal of Intelligent Material Systems and Structures 25 (6) (2014) 697–712.

[40] V. Piefort, Finite element modelling of piezoelectric active structures, Ph.D. thesis, Universite Libre de Bruxelles (2001).

[41] S. Quek, G. Liu, Finite Element Method: A Practical Course, Elsevier

Science, 2003.
[42] A. Preumont, Vibration Control of Active Structures, Springer Netherlands, 2011.
[43] K. Tsubouchi, N. Mikoshiba, Zero-temperature-coefficient saw devices on aln epitaxial films, IEEE Transactions on Sonics and Ultrasonics 32 (5) (1985) 634–644.
[44] M. A. Hopcroft, W. D. Nix, T. W. Kenny, What is the young's modulus of silicon?, Journal of Microelectromechanical Systems 19 (2) (2010) 229–238.
[45] J. Reddy, An Introduction to the Finite Element Method, McGraw-Hill, 2006.
[46] D. Ruiz, J. C. Bellido, A. Donoso, Optimal design of piezoelectric modal transducers, Archives of Computational Methods in Engineering.
[47] E. Andreassen, A. Clausen, M. Schevenels, B. S. Lazarov, O. Sigmund, Efficient topology optimization in matlab using 88 lines of code, Structural and Multidisciplinary Optimization 43 (1) (2011) 1–16.
[48] B. S. Lazarov, O. Sigmund, Filters in topology optimization based on helmholtz-type differential equations, International Journal for Numerical Methods in Engineering 86 (6) (2011) 765–781.
[49] T. H. Lee, Adjoint method for design sensitivity analysis of multiple eigenvalues and associated eigenvectors, AIAA JOURNAL 45 (8) (2007) 1998–2004.
[50] T. D. Tsai, C. C. Cheng, Structural design for desired eigenfrequencies and mode shapes using topology optimization, Structural and Multidisciplinary Optimization 47 (5) (2013) 673–686.

Appendix A. Sensitivity Analysis

The topology optimization problem is solved using an interior point method [30] which requires the gradient of the objective function and the constraints. Let h_1 be the objective function, h_2 be the stiffness constraint, and h_3 be the frequency constraint:

$$h_1(x_d) = K_{uv}^T \phi_1 \left(G_{uu}\phi_1\right)^{-1}, \tag{A.1}$$
$$h_2(x_d) = \phi_1^T K_{uu} \phi_1 \left(G_{uu}\phi_1\right)^{-2}, \tag{A.2}$$
$$h_3(x_d) = \sqrt{\lambda_1}\,(2\pi)^{-1}. \tag{A.3}$$

The computation of the objective and constraints is split into two steps. First structural regularization maps x_d to $\bar{\rho}$, and second the pseudo-densities form a FE model from which the charge sensitivity, stiffness, and frequency values are computed. Lets represent any of h_1, h_2, or h_3 by the function h. The gradient of h is then expressed by the chain rule:

$$\frac{\mathrm{d}h}{\mathrm{d}x_d} = \frac{\mathrm{d}h}{\mathrm{d}\bar{\rho}}\frac{\mathrm{d}\bar{\rho}}{\mathrm{d}x_d}. \tag{A.4}$$

The two RHS terms of Equation (A.4) are derived independently. The subsequent subsections derive the gradient of the regularization operators in Appendix Appendix A.1, the objective in Appendix Appendix A.2, the constraints in Appendix Appendix A.3, and the FE matrices in Appendix Appendix A.4.

Appendix A.1. Gradient of Regularization Operators

The structural regularization is composed of three operators: the symmetry operator G_s, the density filter G_d, and the projection operator $h_p()$. The regularization process be expressed as:

$$\bar{\rho}_a = G_s x_d, \tag{A.5}$$
$$\bar{\rho}_b = G_d \bar{\rho}_b, \tag{A.6}$$
$$\bar{\rho} = h_p(\bar{\rho}_b). \tag{A.7}$$

Being linear, the gradient of the symmetry operator and density filter operator are constant, that is:

$$\frac{\mathrm{d}\bar{\rho}_b}{\mathrm{d}\bar{\rho}_a} = G_d, \tag{A.8}$$
$$\frac{\mathrm{d}\bar{\rho}_a}{\mathrm{d}x_d} = G_s. \tag{A.9}$$

The projection operator is non-linear and diagonal. The gradient of the projection operator needs to be evaluated for each solution at $\bar{\rho}_b$. The gradient of the projection operator is:

$$\frac{\mathrm{d}\bar{\rho}}{\mathrm{d}\bar{\rho}_b} = \frac{\mathrm{d}h_p}{\mathrm{d}\bar{\rho}_b}(\bar{\rho}_b) = \mathrm{diag}\left[\beta\exp(-\beta\bar{\rho}_b) + \exp(-\beta)\right]. \tag{A.10}$$

The gradients of the regularization operators are combined using the chain rule:

$$\frac{\mathrm{d}\bar{\rho}}{\mathrm{d}x_d} = \frac{\mathrm{d}\bar{\rho}}{\mathrm{d}\bar{\rho}_b}\frac{\mathrm{d}\bar{\rho}_b}{\mathrm{d}\bar{\rho}_a}\frac{\mathrm{d}\bar{\rho}_a}{\mathrm{d}x_d}. \tag{A.11}$$

Appendix A.2. Gradient of the Objective Using the Adjoint Method

The evaluation of an eigenvalue problem to compute the objective renders the sensitivity analysis non-trivial. The adjoint method is used to evaluate the gradient of the objective [34, 49, 50]. The sensitivity analysis using the adjoint method considers the objective h_1, the eigenvalue problem g_1, the eigenvector normalization g_2, and the secondary thermal system g_3:

$$h_1(\lambda, \phi, \bar{\rho}, \tau) = K_{uv}^T \phi \left(G_{uu}\phi\right)^{-1}, \tag{A.12}$$
$$g_1(\lambda, \phi, \bar{\rho}, \tau) = \left(K_{uu} - \lambda M_{uu}\right)\phi = 0, \tag{A.13}$$
$$g_2(\lambda, \phi, \bar{\rho}, \tau) = 1 - \phi^T M_{uu}\phi = 0, \tag{A.14}$$
$$g_3(\lambda, \phi, \bar{\rho}, \tau) = K_\tau \tau - \bar{q}_\tau = 0. \tag{A.15}$$

Consider the following Lagrangian function comprised of a linear combination of h_1, g_1, g_2, and g_3:

$$\begin{aligned} L = {} & h_1(\lambda, \phi, \bar{\rho}, \tau) + \alpha^T g_1(\lambda, \phi, \bar{\rho}, \tau) \\ & + \beta g_2(\lambda, \phi, \bar{\rho}, \tau) + \gamma^T g_3(\lambda, \phi, \bar{\rho}, \tau), \end{aligned} \tag{A.16}$$

where α, β, and γ are the adjoint variables. The second, third and fourth terms in Equation (A.16) always evaluate to zero for an eigenvalue, eigenvector, and temperature field of the system. In this case, the Lagrangian function is equal to the objective. Thus the derivative of the Lagrangian is equal to the derivative

of the objective:

$$\begin{aligned}\frac{\mathrm{d}h_1}{\mathrm{d}\bar{\rho}} &= \left(\frac{\partial h_1}{\partial \phi} + \alpha^T \frac{\partial g_1}{\partial \phi} + \beta \frac{\partial g_2}{\partial \phi} + \gamma^T \frac{\partial g_3}{\partial \phi}\right)\frac{\partial \phi}{\partial \bar{\rho}} \\ &+ \left(\frac{\partial h_1}{\partial \lambda} + \alpha^T \frac{\partial g_1}{\partial \lambda} + \beta \frac{\partial g_2}{\partial \lambda} + \gamma^T \frac{\partial g_3}{\partial \lambda}\right)\frac{\partial \lambda}{\partial \bar{\rho}} \\ &+ \left(\frac{\partial h_1}{\partial \tau} + \alpha^T \frac{\partial g_1}{\partial \tau} + \beta \frac{\partial g_2}{\partial \tau} + \gamma^T \frac{\partial g_3}{\partial \tau}\right)\frac{\partial \tau}{\partial \bar{\rho}} \\ &+ \frac{\partial h_1}{\partial \bar{\rho}} + \alpha^T \frac{\partial g_1}{\partial \bar{\rho}} + \beta \frac{\partial g_2}{\partial \bar{\rho}} + \gamma^T \frac{\partial g_3}{\partial \bar{\rho}}.\end{aligned} \tag{A.17}$$

The adjoint variables α, β and γ are found to make the terms in Equation (A.17) containing $\frac{\partial \phi}{\partial \bar{\rho}}$, $\frac{\partial \lambda}{\partial \bar{\rho}}$, and $\frac{\partial \tau}{\partial \bar{\rho}}$ vanish:

$$\frac{\mathrm{d}h_1}{\mathrm{d}\bar{\rho}} = \frac{\partial h_1}{\partial \bar{\rho}} + \alpha^T \frac{\partial g_1}{\partial \bar{\rho}} + \beta \frac{\partial g_2}{\partial \bar{\rho}} + \gamma^T \frac{\partial g_3}{\partial \bar{\rho}}, \tag{A.18}$$

$$\begin{aligned}&= \frac{\partial h_1}{\partial \bar{\rho}} + \alpha^T \left(\frac{\partial K_{uu}}{\partial \bar{\rho}} - \lambda \frac{\partial M_{uu}}{\partial \bar{\rho}}\right)\phi \\ &- \beta \phi^T \frac{\partial M_{uu}}{\partial \bar{\rho}}\phi + \gamma^T \left(\frac{\partial K_\tau}{\partial \bar{\rho}}\tau - \frac{\partial \overline{q}_\tau}{\partial \bar{\rho}}\right).\end{aligned} \tag{A.19}$$

The derivatives of the FE matrices are analyzed in Appendix Appendix A.4. The terms in Equation (A.17) containing $\frac{\partial \phi}{\partial \bar{\rho}}$, $\frac{\partial \lambda}{\partial \bar{\rho}}$, and $\frac{\partial \tau}{\partial \bar{\rho}}$ vanish for adjoint variables evaluated from the adjoint equations:

$$\begin{bmatrix} K_{uu} - \lambda M_{uu} & -2M_{uu}\phi & 0 \\ -\phi^T M_{uu} & 0 & 0 \\ 0 & 0 & K_\tau \end{bmatrix} \begin{bmatrix} \alpha \\ \beta \\ \gamma \end{bmatrix} = \begin{bmatrix} -\frac{\partial h_1}{\partial \phi}^T \\ -\frac{\partial h_1}{\partial \lambda}^T \\ -\frac{\partial h_1}{\partial \tau}^T \end{bmatrix}. \tag{A.20}$$

For the objective employed in this work, the partial derivatives of $h_1(\lambda, \phi, \rho, \mu)$ are:

$$\frac{\partial h_1}{\partial \bar{\rho}} = \frac{\partial K_{uv}^T}{\partial \bar{\rho}}\phi \left(G_{uu}\phi\right)^{-1}, \tag{A.21}$$

$$\frac{\partial h_1}{\partial \phi} = \left(K_{uv}^T (G_{uu}\phi) - G_{uu}(K_{uv}^T \phi)\right)\left(G_{uu}\phi\right)^{-2}, \tag{A.22}$$

$$\frac{\partial h_1}{\partial \lambda} = 0, \tag{A.23}$$

$$\frac{\partial h_1}{\partial \tau} = \frac{\partial K_{uv}^T}{\partial \mu}\phi \left(G_{uu}\phi\right)^{-1} G_\tau. \tag{A.24}$$

G_τ is a linear operator that maps τ to μ. Its action is described by Equation (40). Considering the analysis presented in this section, the process of evaluating the gradient of the objective is:

1. Build the sparse linear system in Equation (A.20).
2. Solve for the adjoint variables using an iterative algorithm for sparse systems.
3. Evaluate the Equation (A.19) for the gradient of the objective.

Appendix A.3. Gradient of the Constraints

The adjoint method is used to evaluate the gradient of the stiffness and frequency constraint. The analysis of Appendix Appendix A.2 is used to derive the gradient with stiffness constraint h_2:

$$h_2(\lambda, \phi, \bar{\rho}, \tau) = \phi^T K_{uu}\phi \left(G_{uu}\phi\right)^{-2}. \tag{A.25}$$

The differences in the analysis result from the evaluation of the partial derivatives of h_2:

$$\frac{\partial h_2}{\partial \bar{\rho}} = \phi^T \frac{\partial K_{uu}}{\partial \bar{\rho}}\phi \left(G_{uu}\phi\right)^{-2}, \tag{A.26}$$

$$\frac{\partial h_2}{\partial \phi} = 2\phi^T K_{uu} \left(G_{uu}\phi\right)^{-2} - 2k_1 G_{uu} \left(G_{uu}\phi\right)^{-1}, \tag{A.27}$$

$$\frac{\partial h_2}{\partial \lambda} = 0, \tag{A.28}$$

$$\frac{\partial h_2}{\partial \tau} = \phi^T \frac{\partial K_{uu}}{\partial \mu}\phi \left(G_{uu}\phi\right)^{-2} G_\tau. \tag{A.29}$$

With these partial derivatives, Equation (A.20) is constructed and solved then Equation (A.19) is evaluated, with h_2 substituted for h_1. For the frequency constraint $h_3(\lambda, \phi, \bar{\rho}, \tau) = \sqrt{\lambda}/2\pi$, the partial derivatives are:

$$\frac{\partial h_3}{\partial \bar{\rho}} = \frac{\partial h_3}{\partial \phi} = \frac{\partial h_3}{\partial \tau} = 0, \tag{A.30}$$

$$\frac{\partial h_3}{\partial \lambda} = \frac{1}{4\phi\sqrt{\lambda}}. \tag{A.31}$$

Appendix A.4. Gradients of the Finite Element Matrices

Every element in the electromechanical model has identical material properties prior to the penalization. The penalization of the material properties from the C-SIMP material model is applied during the the assembly of the FE matrices as follows:

$$K_{uu} = \sum_i e^{-q_e \mu_i} \bar{\rho}_i^{\,p_e} \mathrm{assem}_i(K_{uu}^e), \tag{A.32}$$

$$K_{uv} = \sum_i e^{-q_p \mu_i} \bar{\rho}_i^{\,p_p} \mathrm{assem}_i(K_{uv}^e), \tag{A.33}$$

$$K_{vv} = \sum_i e^{-q_c \mu_i} \bar{\rho}_i^{\,p_c} \mathrm{assem}_i(K_{vv}^e), \tag{A.34}$$

$$M_{uu} = \sum_i e^{-q_d \mu_i} \bar{\rho}_i^{\,p_d} \mathrm{assem}_i(M_{uu}^e), \tag{A.35}$$

where the summation is over all elements in the FE model. The FE matrices are a linear combination of constant matrices. The coefficients of the linear combination are a function of the pseudo-densities and connectivity penalties. The derivatives with respect to the i^{th} pseudo-density and connectivity penalty, for example with K_{uu}, are:

$$\frac{\partial K_{uu}}{\partial \bar{\rho}_i} = p_e \exp(-q_e \mu_i) \bar{\rho}_i^{\,p_e - 1} \mathrm{assem}_i(K_{uu}^e), \tag{A.36}$$

$$\frac{\partial K_{uu}}{\partial \mu_i} = -q_e \exp(-q_e \mu_i) \bar{\rho}_i^{\,p_e} \mathrm{assem}_i(K_{uu}^e). \tag{A.37}$$

Similar expression are derived for the other FE matrices.